batteries

MDPI

*Article*

# Electrode-Level Emulation of Temperature Impact in Commercial Li-Ion Batteries

**Matthieu Dubarry *, Alexa Fernando and David Beck**

Hawai'i Natural Energy Institute, University of Hawai'i at Mānoa, Honolulu, HI 96815, USA; dmbeck@hawaii.edu (D.B.)

* Correspondence: matthieu@hawaii.edu

**Abstract**

Temperature affects the battery voltage response, and it is essential to take this influence into consideration for diagnosis purposes, as it could be misinterpreted for degradation. Temperature affects cell kinetics, and a good proxy to emulate this impact is to use electrode data at different C rates. This work further validates this concept by analyzing the relationship between temperature and rate at the electrode level for commercial graphite//$LiFePO_4$ and (silicon, graphite)//$LiNi_{0.8}Mn_{0.1}Co_{0.1}O_2$ cells. It will be shown that excellent emulation accuracy for both the voltage response and the capacity retention can be obtained for temperatures varying between −14 °C and 55 °C.

**Keywords:** temperature; incremental capacity; LFP; NMC811; degradation modes

## 1. Introduction

Because of the path dependency of battery degradation [1–3], the aging of any deployed battery is going to be unique and, as a result, there is a need for onboard diagnosis and prognosis. The merits of different state-of-health tracking methodologies have been extensively covered in multiple reviews in recent years [4–8], and it is important to realize that their accuracy will heavily depend on the information provided by the different sensors embedded in the battery packs. For voltage-based methods, it is essential to take temperature and C rate into consideration, as they are known to influence the voltage response of the cell [9], and thus the interpretability of the reported values will be significantly influenced by how well the diagnosis algorithm can separate the variations associated with aging and those associated with temperature or rate [9].

On a more fundamental level, understanding and being able to model the impact of temperature on the voltage and performance of a cell is also essential to be able to properly simulate large cells or battery packs in which temperature gradients are common [10–21] and have been shown to significantly influence the overall voltage response and ultimately cell degradation.

The modeling of the impact of temperature in lithium-ion batteries is a vast topic where multiple approaches have already been reported [22–30]. Unfortunately, most of them require extensive parameterization and computing resources, which make them impractical for onboard BMS. Lighter modeling approaches, such as Degradation modes models [31–34], have also been proven to account for temperature using the impact of rate as a proxy [31,35]. These models offer the advantage of fast calculations and easy parameterization with just five parameters on top of half-cell data for each electrode (or each component of the electrodes for blends): two that are thermodynamic (the ratio of the

Check for updates

Academic Editor: Pascal Venet

Received: 30 March 2026
Revised: 5 May 2026
Accepted: 12 May 2026
Published: 16 May 2026

**Copyright:** © 2026 by the authors. Licensee MDPI, Basel, Switzerland. This article is an open access article distributed under the terms and conditions of the Creative Commons Attribution (CC BY) license.

electrode capacities and their slippage), and three related to kinetics (the resistance and rates of each electrode) [31,36].

The link between C rate and temperature was proposed in 2012 [31] and validated a few years later [35]. In a recent work, it was also demonstrated that this approach can be applied at the full-cell level without the need for any modeling [37] by matching the response at different temperatures to the response at different rates using only a resistance correction. This work showcased a clear relationship between rate and temperature, with lower temperatures being emulable from higher rates and inversely for higher temperatures and lower rates. However, there was a major caveat: while voltages were replicated well, estimating capacity retention was less successful. This work is a follow-up study where the same dataset as in [37] was fitted using a degradation modes model, using electrode data harvested from the same commercial cells. This dataset was composed of two commercial cells comprising different positive electrode (PE) chemistries, lithium iron phosphate (LFP) and a nickel manganese cobalt oxide (NMC), tested at two different rates and temperatures ranging from −14 °C to 55 °C. This work establishes that performing the temperature/rate matching at the electrode level allows for emulating both the voltage and capacity retention changes associated with both increasing and decreasing temperatures. It also demonstrates that the variation in kinetic parameters can be summarized by a single chemistry-dependent set of parameters that will enable extending the results to other rates and temperatures. While the origin of this relationship is out of the scope of this work, our results should facilitate the applicability of the degradation modes approach to deployed cells where the temperature or rate cannot be controlled.

## 2. Materials and Methods

Two types of commercially available 18650 full-cell lithium-ion batteries were used in this work, one graphite intercalation compound (GIC)/LFP 1.1 Ah cell (APR18650M1B, LithiumWerks, Round Rock, TX, USA) and a Si, GIC/NMC811 3.5 Ah cell (INR18650MJ1, LG Chem, Seoul, Republic of Korea), similar to our previous work [35–37]. No new full-cell data was generated for this work; the full-cell results and detailed protocol have already been published elsewhere [35] and will not be repeated here. Testing was performed at C/10 and C/3 in increments of 3 °C between −14 °C and 55 °C.

Half-cells were assembled from the positive and negative electrodes (PE and NE, respectively) harvested from the full-cells. One cell of each chemistry was discharged to 2 V before being opened in a glove box. After the unrolling of the jellyroll, one side of each of the electrode sheets was partially scrubbed with N-methyl-2-pyrrolidone to reveal the current collector before a 1.8 cm diameter piece was cut out for testing. Coin cells were assembled using the harvested electrodes and 0.25 mm thick metallic lithium chips acting as the counter and reference electrode with a 260 µm glass fiber separator. The electrolyte was prepared in-house following the protocol proposed in [19]. This electrolyte was designed for minimizing resistance and was composed of ethylene carbonate, dimethyl carbonate, diethyl carbonate, ethyl methyl carbonate, and propylene carbonate in a 20/40/10/15/15 volumetric ratio with 1.25 M lithium hexafluorophosphate as the salt. Vinylene carbonate and fluoroethylene carbonate were added as additives at 3% per weight each. Half-cell characterizations were performed using either an MPG-200 Series or VMP-3 battery cycler. MPG-200 and VMP-3 have a controlled voltage range between 0 V and 5 V (100 µV accuracy) and a controlled current range between 10 µA and 100 mA (0.1% control accuracy).

After three formation cycles at C/10, all the cells but the NMC NE performed one cycle at C/50, C/25, C/10, C/5, C/2, C/1, 1.5C, 2C, 3C and 4C, where each half-cycle was followed by a 4 h rest and a residual capacity step at C/50 under the same regime before another 4 h rest to ensure full completion and equilibrium before the next step [38]. The

NMC NE used the same protocol but was cycled at C/50, C/25, C/15, C/10, C/5, C/2, C/1, and 2C (charge only for the latter). The LFP PE was cycled between 2 V and 3.8 V, and the NMC811 PE from 3 V to 4.3 V. Both NEs were cycled up to 1 V and used a gradually decreasing cutoff voltage in discharge to fully discharge the negative electrode, accounting for polarization while being careful not to go low enough in voltage to induce lithium plating [39]. The discharges cutoffs were −4 mV at C/50, −4.6 mV at C/25, −15 mV at C/5, −24 mV at C/2, −43 mV at C/1, −52 mV at 1.5C, −62 mV at 2C, −89 mV at 3C, and −116 mV at 4C for the LFP NE and of −4 mV at C/50, −4.7 mV at C/25, −5 mV at C/15, −8 mV at C/10, −15 mV at C/5, −24 mV at C/2, and −44 mV at C/1 for the NMC NE.

Simulations were performed using the 'alawa toolbox [29,40] using the electrode data gathered through the half-cell testing. The initial matching of the electrodes was performed using the data at C/25 to enable kinetic difference accommodation between the full-cell and the half-cells using the rate degradation factor (RDF). For this matching, the RDF lower limit was set at 0.5, which indicates that the data down to half the requested rate could be used for the simulation, i.e., C/50 in lieu of C/25 [29,35], matching the lower tested rate. The upper limit was set at 5, i.e., C/5 used instead of C/25. This matching was used to set the two main model parameters for each chemistry, the loading ratio (LR) and the offset, which were both considered constant throughout this study. For simplicity, the NE for the NMC cell was used instead of emulating a blended electrode between GIC and Si, since our previous work showed that the Si signature disappeared quickly when the temperatures were lowered [35]. Parameter estimation for the data at different temperatures was performed by varying the model kinetic parameters: the RDF for both electrodes ($RDF_{PE}$ and $RDF_{NE}$ for the PE and NE, respectively) and the ohmic resistance increase (ORI). Since the model cannot differentiate between resistance increase at the PE or NE, it was assumed to be similar on both electrodes. The RDFs were allowed to vary between limits set by the slowest and highest rate during testing, which corresponded to 0.2 to either 40 or 10 for the C/10 cycles, depending on the fastest performed rate (4C or C/1), and to 0.06 to either 12 or 3 for the C/3 cycles. Best candidates were identified from a mix of manual fits, optimums deciphered from root mean square error calculation between the experimental and simulated voltage responses, as well as normalized capacity comparisons.

## 3. Results

Figure 1 presents the results for the half-cell testing for all four electrodes in charge and discharge. The PE harvested from the LFP cell, Figure 1a, showcased the typical LFP signature with mainly a voltage plateau whose slope increased with increasing rate, especially in discharge. The capacity retention at 4C was found to be around 50% in both charge and discharge. The associated NE, Figure 1b, also showcased good capacity retention at 4C, about 40% in discharge and close to 90% in charge. Figure 1b also highlights the benefits of using varying discharge cutoffs for the NE, as the 4C capacity in discharge would have only been around 15% if a 0 V cutoff was used. The half-cell data for the NMC PE is presented in Figure 1c. It showcases the typical NMC811 signature for the low rates, but quickly loses capacity in charge and discharge when the rate increases, showcasing that this cell was likely optimized for energy rather than power. Rates above 1.5C presented some anomalies at the beginning of charge, also likely linked with the high-energy setting.

The NMC cell NE, Figure 1d, also presented limited capacity retention for the higher rates, confirming the high-energy configuration and explaining why rates above 1C in discharge and 2C in charge were not performed. The additional plateau observed around 0.8 V for the 2C charge might be associated with the formation of the $Li_{15}Si_4$ phase [38]. This phase is typically kinetically constrained and is not expected to occur at a lower

temperature, which might affect the outcome of the model for $RDF_{NE}$s > 3, where the model would interpolate between the data at C/1 and the data at 2C to simulate a C/3.

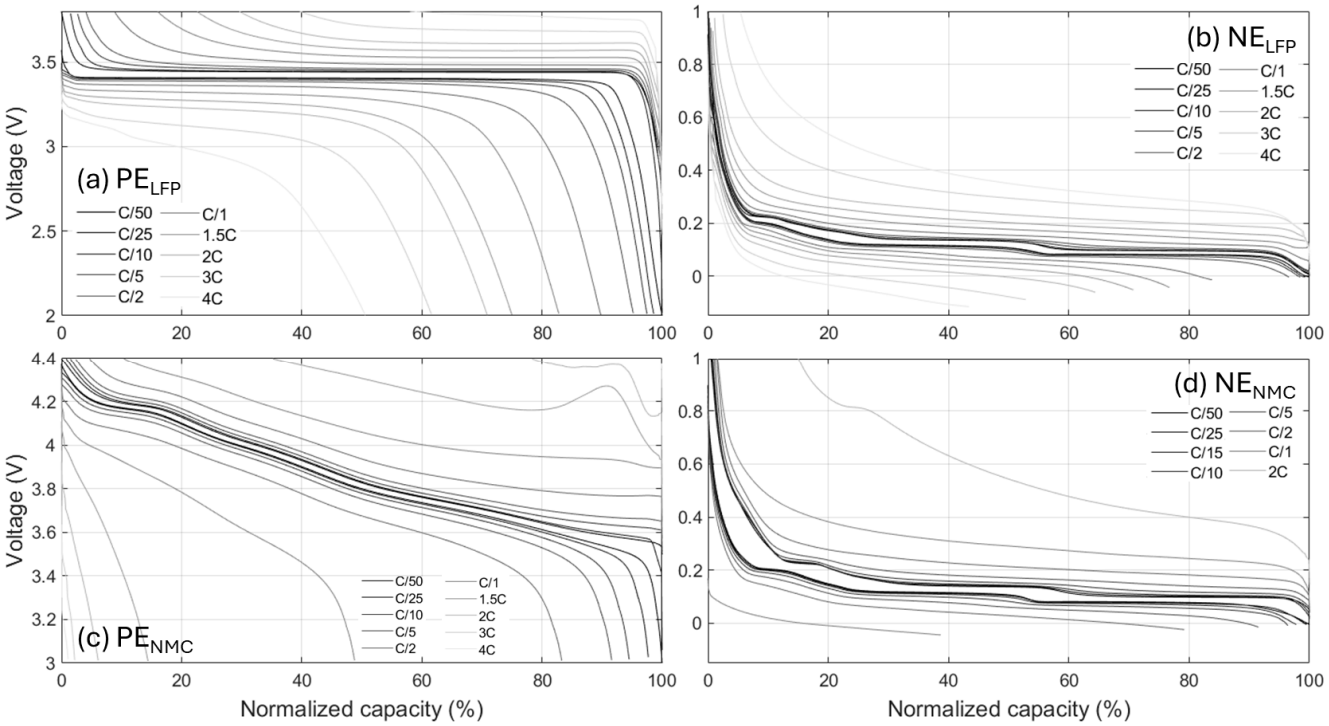


**Figure 1.** Results from the half-cell testing in charge and discharge for (**a**) $PE_{LFP}$, (**b**) $NE_{LFP}$, (**c**) $PE_{NMC}$, and (**d**) $NE_{NMC}$.

Figure 2 presents the emulation results for the room-temperature C/25 charge and discharges for (a) the LFP and (b) the NMC cells with peak indexation following the literature [39]. For the LFP cell, Figure 2a, the emulation showcased good agreement with the experimental data for all peaks in both charge and discharge with an LR of 1.18 and an offset of 9%. This high LR and offset is pretty typical of an LFP cell, where there is often a higher NE excess and low initial capacity loss on the PE [39]. The resistance correction was estimated at −0.15, and the RDFs at 0.5 and 0.6 for the PE and the NE, respectively, which likely reflects the difference in electrolyte and separators between the half-cell and the full cell. For the NMC cell, Figure 2b, there is also a good agreement for all the peaks, with the exception of the one associated with silicon (❷$_{Si}$★③), which is lower for the emulated cell. This discrepancy might be associated with the fact that the cell was opened several months after the testing of the full-cell and that it therefore experienced calendar aging, which is known to affect more silicon than graphite [40,41]. The obtained LR was lower than that of the one obtained for the LFP cells (0.91 vs. 1.18), which was expected given the high energy setting. While this value might appear low, especially since it is below 1, it is important to remember that this is not the N/P ratio. Two main factors can explain the differences between LR and the typical N/P ratio: first, the LR reflects the relationship between the PE and NE after the formation of the solid electrolyte interphase and, second, it is also influenced by the tested voltage window. In this case, the PE was tested up to 4.4 V and therefore appears larger compared to the NE. The offset was estimated at 7.5%, the resistance correction was −0.1 and the RDFs were 0.5 and 1 for the PE and the NE, respectively.

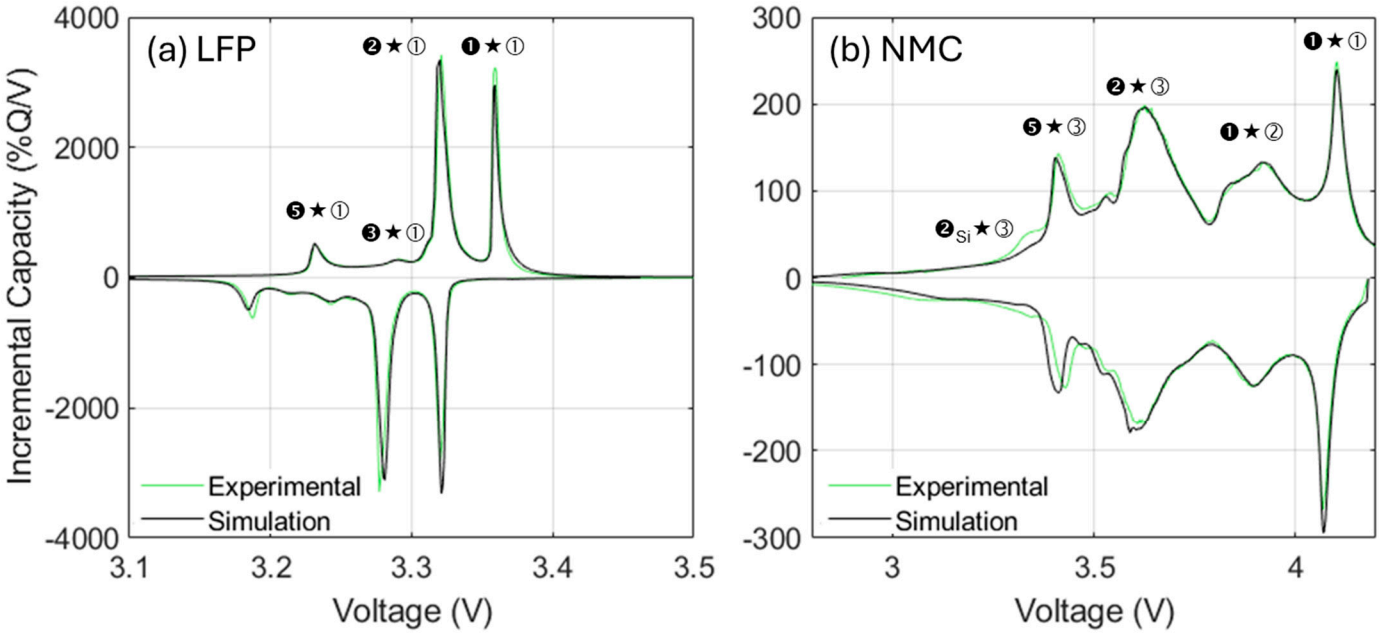


**Figure 2.** Emulation results from the room-temperature C/25 charges and discharges for (**a**) the LFP and (**b**) the NMC cells. The ★ indicates a convolution between peaks associated with the NE (black number) and the PE (white number) [31,39].

Figure 3 presents the results of electrode matching for the LFP cell using the half-cell data gathered at room temperature. A close-up of the electrochemical data is provided in Figure A1. Overall, an excellent replication of the electrode response of the cell at temperatures ranging from −14 °C to 55 °C was obtained by varying the RDFs for both electrodes and the ORI, Figure 3a–d, independently of the regime and the rate. In all cases, the position and shape changes for all electrochemical peaks visible on the IC signature were closely reproduced. The parameters associated with the simulations are presented in Figure 3e–g. The evaluation of the RDFs with temperature was plotted as an Arrhenius plot following our recent results [35,37]. For the PE, the logarithm of the $RDF_{PE}$ was found to decrease linearly with the inverse of the temperature for all conditions and with a similar slope, but there was a separation between the charge and discharge curves, with higher $RDF_{PE}$ for the discharges. The constant values correspond to the lower limit of the $RDF_{PE}$ set by the experimental conditions. As explained in the Materials and Methods section, this limit is rate-dependent and lower for C/3 because slower rates were available compared to C/10. For the NE, there also seems to be a linear relationship between the logarithm of $RDF_{NE}$ and the inverse of the temperature, but with a lower slope than that observed for $RDF_{PE}$. There was also a separation between the charge and discharge curves, with lower values for the discharges. This flip, compared to $RDF_{PE}$, is not surprising, since the full cell discharge corresponds to a charge on the NE. Therefore, the evolution is similar on both electrodes, with higher kinetic limitations in their discharge. Figure 3g presents the evolution of the ORI with different responses for charge, discharge, and rates. In discharge, the fits did not showcase any significant variations with temperature, but the resistance correction was higher for C/3 than for C/10. This is also true in charge, but this time the resistance correction decreases with increasing temperature, with slopes that appear close. Finally, Figure 3f presents the comparison of the simulated capacities versus the experimental ones, showcasing excellent agreement for all rates and regimes, with all values close to the black 1:1 line.

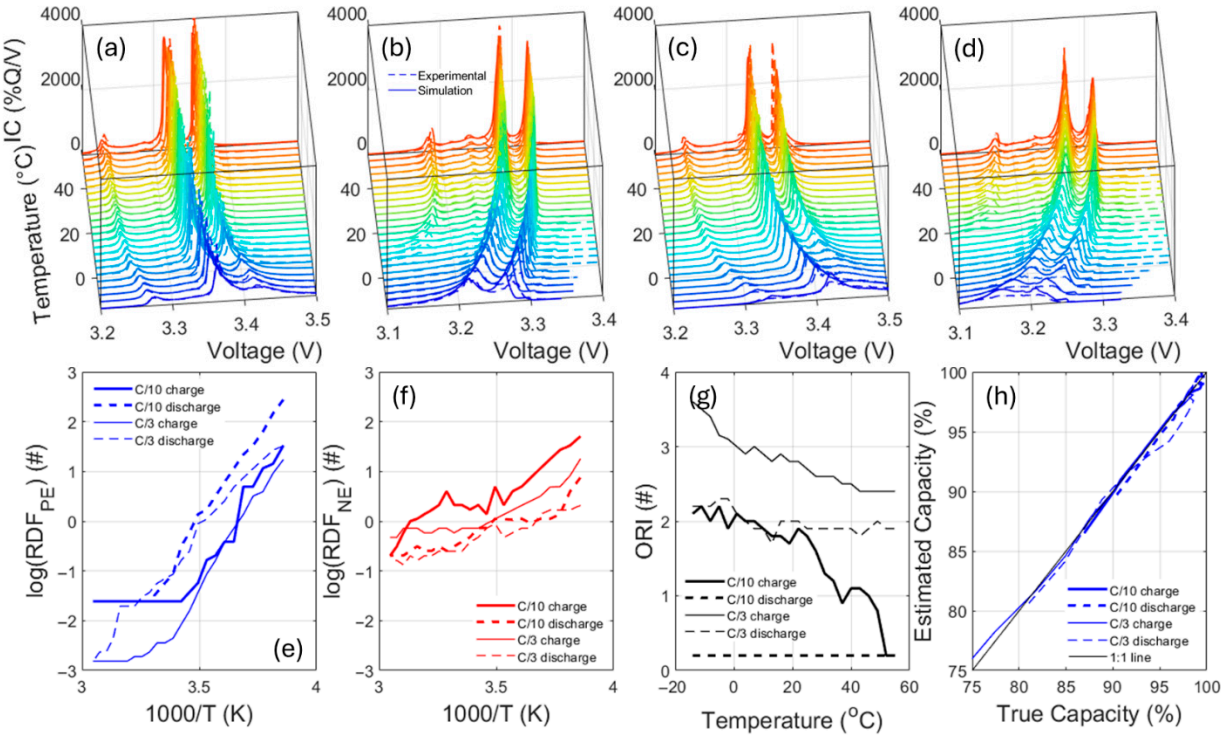


**Figure 3.** Fitted temperature emulation results with associated parameter variations for the LFP cell. IC signatures for the experimental (dashed lines) and simulated (full lines) (**a**) C/10 charges, (**b**) C/10 discharges, (**c**) C/3 charges, and (**d**) C/3 discharges with associated (**e**) $RDF_{PE}$, (**f**) $RDF_{NE}$, (**g**) ORI, and (**h**) capacity estimations vs. true capacity, with a 1:1 line in black.

Figure 4 presents the same results for the NMC cell. A close-up of the electrochemical fits is provided in Figure A2. Once again, the best fits matched well with the voltage experimental variations, both at C/10 (Figure 4a,b) and C/3 (Figure 4c,d), whether in charge (Figure 4a,c) or discharge (Figure 4b,d), although it has to be noted that, for the C/3 charge, the best fit for the −14 °C data (darkest blue) is not quite satisfactory, as it includes significant lithium plating (* on Figure 4c). This can likely be explained in part by the fact that the resistance of the half-cell NE was higher than that of the full-cell because of the size difference [42]. As such, the NE potential would be lower in the half-cell, and the discharges were thus more likely to be incomplete during testing, despite our efforts to lower the cutoff voltages below 0. This likely could be solved by gathering the half-cell data on larger electrodes.

Looking at the evolution of the fitted parameters, Figure 4e–f, the RDFs were again found to follow an Arrhenius relationship, with a larger slope for the PE than for the NE. No clear difference is visible between the charge and discharge, but some is visible between the C/10 and C/3 fits, with slightly lower slopes for the faster rate. The resistance correction estimations were dispersed without any clear trends between the experiments, as shown in Figure 4g. Finally, the predicted capacity loss, Figure 4h, was close to the 1:1 line compared to the experimental one, but there were more deviations compared to the LFP results, especially for the higher losses. This could be associated with the fact that the kinetic impact of the graphite and the silicon portions of the electrode was not separated. In addition, while the potential presence of the $Li_{15}Si_4$ phase [38] did not seem to have played a major role in the capacity estimation, as the estimated capacities for the low temperature C/3 discharges were actually lower than the true ones, it might have influenced their voltage emulation, which were the furthest from the experimental data.

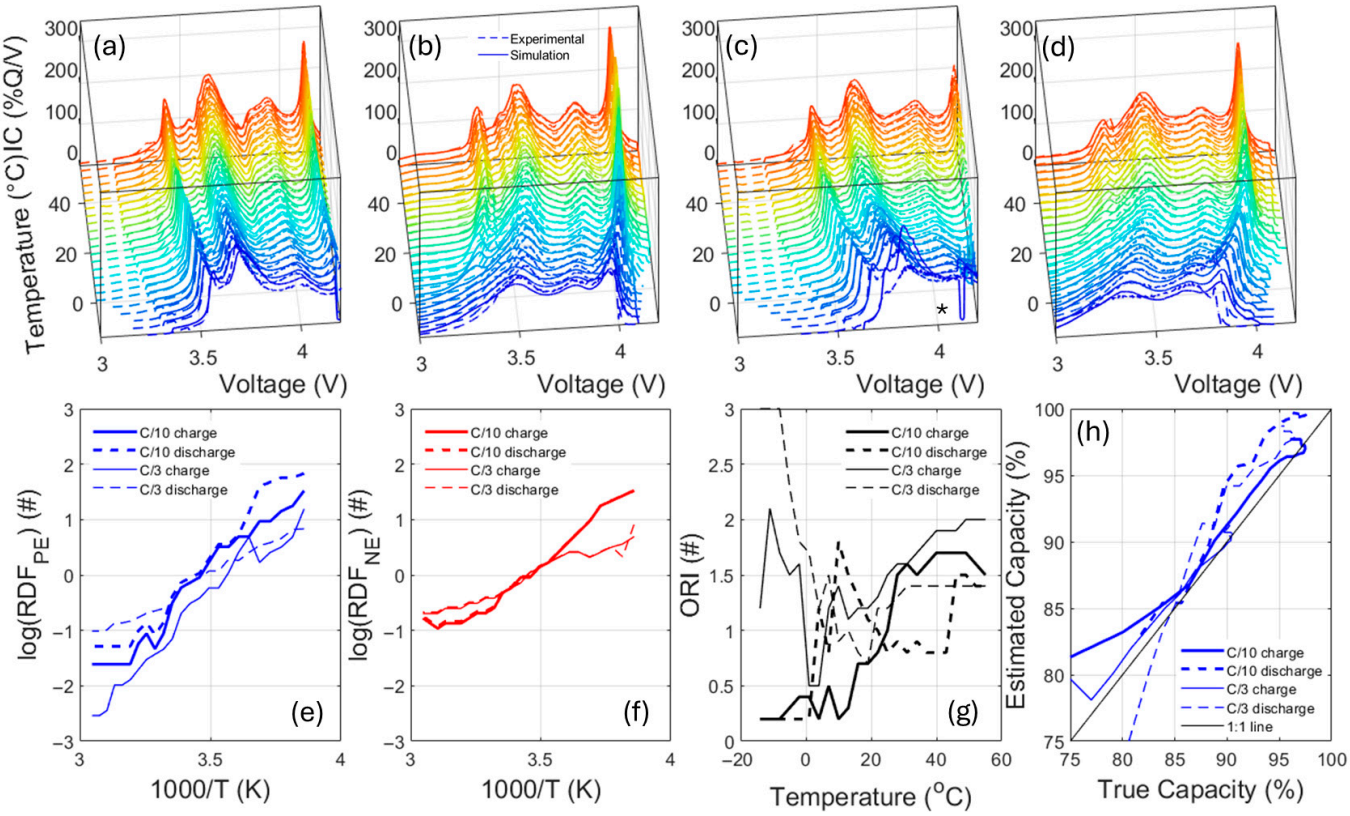


**Figure 4.** Fitted temperature emulation results with associated parameter variations for the NMC cell. IC signatures for the experimental (dashed lines) and simulated (full lines) (**a**) C/10 charges, (**b**) C/10 discharges, (**c**) C/3 charges, and (**d**) C/3 discharges with associated (**e**) $RDF_{PE}$, (**f**) $RDF_{NE}$, (**g**) ORI, and (**h**) capacity estimations vs. true capacity, with a 1:1 line in black. The * indicates lithium plating.

## 4. Discussion

Given the results of individual matchings at all rates and temperatures, Figures 3 and 4, and as previously deciphered [35], it is clear that the voltage and capacity changes associated with temperature can be inferred from the room-temperature data by varying the RDF for both electrodes and the ORI. Similar to what was observed before [35,37], the RDFs seemed to follow an Arrhenius relationship with temperature. This might not be the case for the ORI, which seems to follow a linear trend with temperature, in agreement with our work on similar cells at the full-cell level [37]. However, in contrast to the difference in what was observed at the full-level level, where only a few comparisons were possible, there might be much more impact of rate and regime at the electrode level, which could complicate implementation. Indeed, at least a rate-independent relationship is desirable to be able to perform simulations at different rates and temperatures from a simple calibration. While some differences can be observed in Figures 3 and 4, it is unclear if their impact on the voltage response of the full cell is significant. To test this hypothesis, Figures 5 and 6 present our best attempts to use a single set of parameters to represent the entire temperature space. For the LFP cell, Figure 5, the RDFs and ORI were calculated using the average RDF slopes in addition to the resistance variations associated with the higher rate. For the NMC cell, the best overall results were obtained using the slopes associated with the higher rate, as shown in Figure 6. Having a unique parameter enables a comparison of the RDF and capacity variations to those obtained at the full cell level [37] (green curves), with the exception of the ORI, which is not comparable.

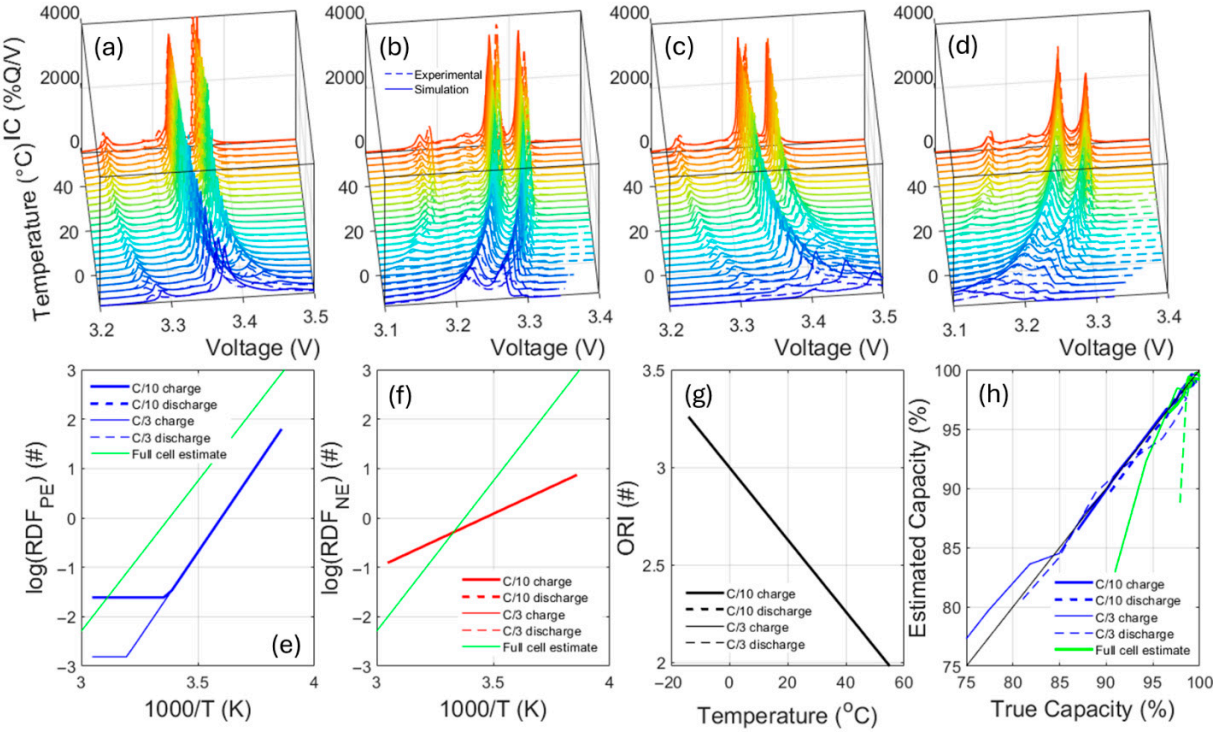


**Figure 5.** Best overall simulated temperature emulation results with associated parameter variations for the LFP cell. IC signatures for the experimental (dashed lines) and simulated (full lines) (**a**) C/10 charges, (**b**) C/10 discharges, (**c**) C/3 charges, and (**d**) C/3 discharges with associated (**e**) $RDF_{PE}$, (**f**) $RDF_{NE}$, (**g**) ORI, and (**h**) capacity estimations vs. true capacity, with a 1:1 line in black. Green lines correspond to the parameters deciphered at the full-cell level in [37].

For the LFP cell, the obtained voltage responses using average slopes, while not as good as the one obtained under individual fits (Figure A3), did not showcase any major differences compared to their experimental counterparts, as shown in Figure 5a–d, especially in their charge. For the RDFs, the slope determined from the full-cell matching (green curve) was similar to that of the most kinetically limited electrodes, the PE. In addition, the matching at the electrode level enabled good estimation of the capacity loss as a function of temperature, which was not the case at the full-cell level (green curves in Figure 5h), where the capacities deviated by up to 7% for lower temperatures.

For the NMC cell, using the average values overestimated the RDFs at lower temperatures (Figure A4). Using the slopes associated with the higher rate instead (Figure 6) allowed better replication of the electrochemical behavior, although some significant plating is predicted at low temperature for C/3 charges (Figure 6c). In contrast to the LFP cell, the $RDF_{PE}$ evolution was not similar to that observed on the full-cell [37], Figure 6e, with the slopes between the PE and NE being much closer (Figure 6f). In addition, the best fits were obtained with an ORI that increases with temperature rather than decreases (Figure 6g). It is important to remember that the ORI is not a straight resistance but a resistance correction applied to different rates, which is intricately linked to the RDF evolution [31]. This implies that, contrary to what was observed for the LFP cell, and at a similar kinetic hindrance, the rate-induced polarization was lower than that of the temperature-induced polarization. Regarding the capacity estimations, while not perfect, they were still better than the one predicted from the full-cell analysis (green curves in Figure 6h), where the capacities deviated by up to 7%.

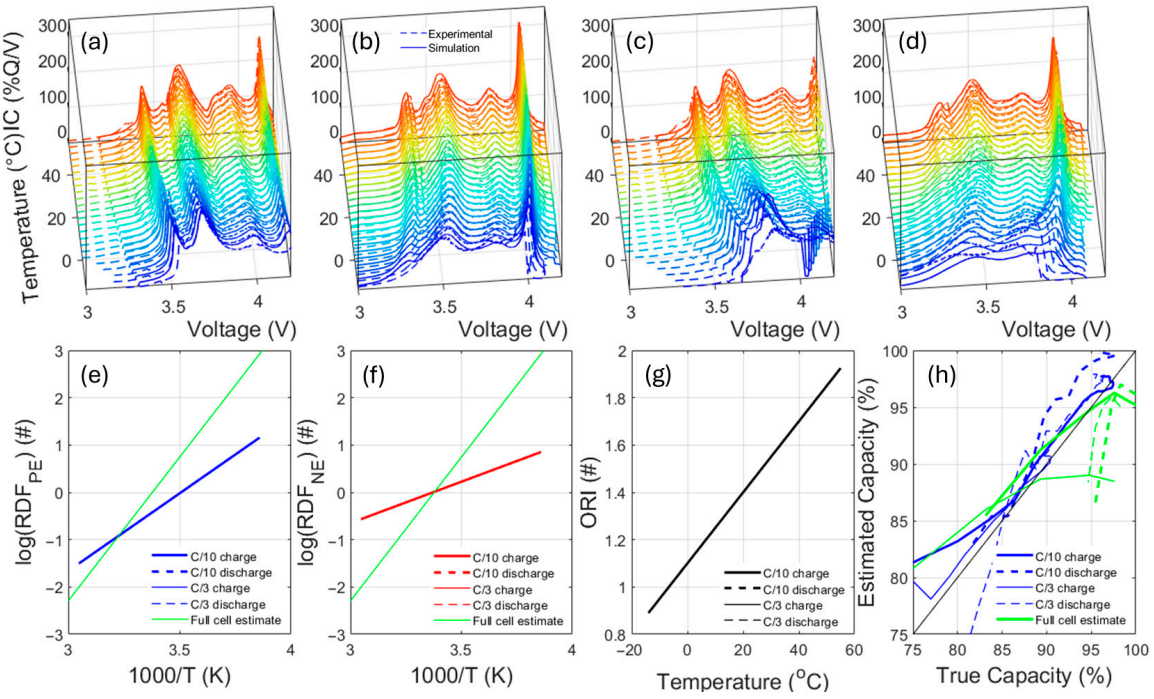


**Figure 6.** Best overall simulated temperature emulation results with associated parameter variations for the NMC cell. IC signatures for the experimental (dashed lines) and simulated (full lines) (**a**) C/10 charges, (**b**) C/10 discharges, (**c**) C/3 charges, and (**d**) C/3 discharges with associated (**e**) $RDF_{PE}$, (**f**) $RDF_{NE}$, (**g**) ORI, and (**h**) capacity estimations vs. true capacity, with a 1:1 line in black. Green lines correspond to the parameters deciphered at the full-cell level in [37].

The origin of the performance difference between our approach for the NMC-based cell and LFP-based ones might be related to heat generation. According to the literature, NCM-based cells could generate more heat than LFP-based ones [43,44]; therefore, the temperature of the electrodes might vary significantly throughout charge and discharge. In addition, this heat generation is also state of charge (SOC)-dependent, which implies that its impact on the voltage response might not be straightforward. Since our approach only considers the impact of temperature on the full regime at once, it does not account for this effect, which likely affects the quality of the fits, e.g., the plating observed for the low temperatures for the NMC cell might not have happened experimentally if the kinetics were improved because of an increase in the internal temperature toward the end of charge. This will be investigated in future work by introducing an SOC-dependent RDF correction.

## 5. Conclusions

This study demonstrated in more detail the intricate relationship between rate and temperature at the electrode level, and that one can be used to emulate the other. The rate degradation factors on both the positive and negative electrodes were found to follow an Arrhenius relationship with temperature and the resistance correction to follow a linear relationship. While the best fits showcased the impact of rate and regime on all three parameters, a unique slope for each electrode and chemistry was found to be able to replicate both the voltage response in temperature as well as the associated capacity retention. This is an improvement over our previous work at the electrode level, which provided good voltage estimations but lacked the ability to predict the associated capacity loss consistently. This highlights that accounting for electrode-specific kinetic limitations is necessary to accurately reflect the impact of temperature.

Having a single set of parameters enabling the emulation of all the temperatures from room-temperature data should enable extending the results to other rates and temper-

atures and enable better integration of the impact of temperature and rate for onboard diagnostics. It should also enable better simulation of large cells or battery packs with temperature gradients.

**Author Contributions:** Conceptualization, M.D.; methodology, M.D.; software, M.D.; experimentation, A.F. and D.B.; validation, M.D.; formal analysis, M.D.; investigation, M.D.; resources, M.D.; data curation, M.D.; writing—original draft preparation, M.D.; writing—review and editing, A.F., D.B. and M.D.; visualization, M.D.; supervision, M.D.; project administration, M.D.; funding acquisition, M.D. All authors have read and agreed to the published version of the manuscript.

**Funding:** This research was funded by ONR grant number N00014-25-1-2372.

**Data Availability Statement:** The full-cell data was previously published in [35]. Licensing for the modeling toolbox is free for academic use; see [45] for more details. The half-data used for this work will be made available upon reasonable request at the discretion of the authors.

**Conflicts of Interest:** The authors declare no conflicts of interest.

## Abbreviations

The following abbreviations are used in this manuscript:

| | |
|---|---|
| GIC | Graphite intercalation compound. |
| LFP | Lithium iron phosphate. |
| LR | Loading ratio. |
| NMC | Nickel manganese cobalt oxide. |
| NE | Negative electrode. |
| ORI | Ohmic resistance increase. |
| PE | Positive electrode. |
| RDF | Rate degradation factor. |
| SOC | State of charge. |

## Appendix A

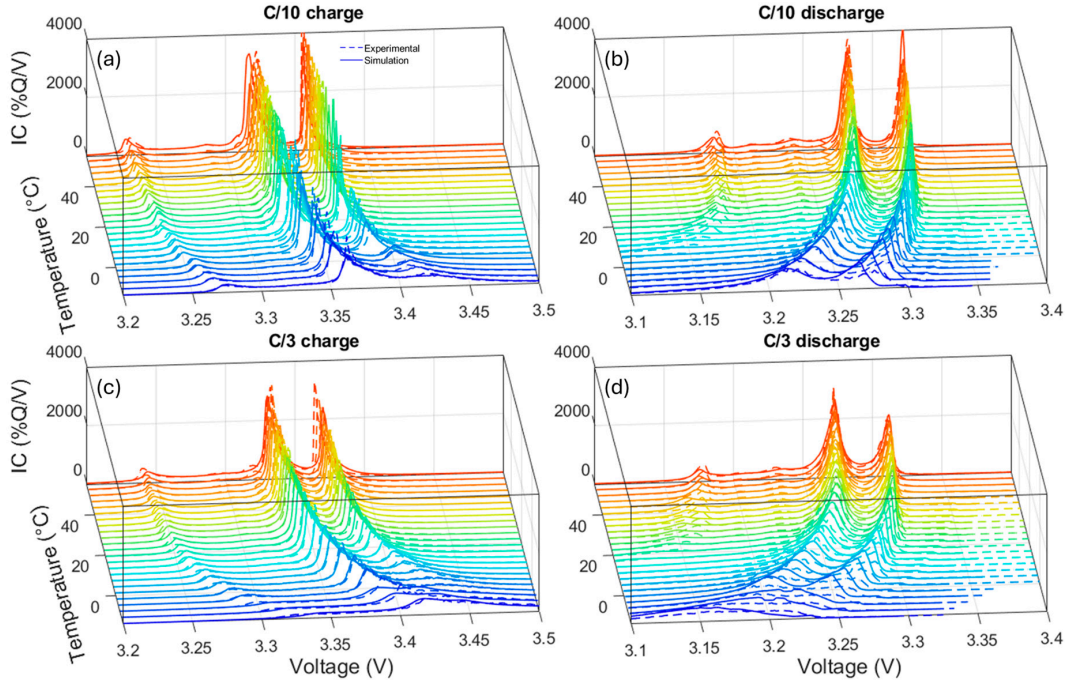


**Figure A1.** LFP cell IC signatures comparison for the experimental (dashed lines) and simulated (full lines) (**a**) C/10 charges, (**b**) C/10 discharges, (**c**) C/3 charges, and (**d**) C/3 discharges.

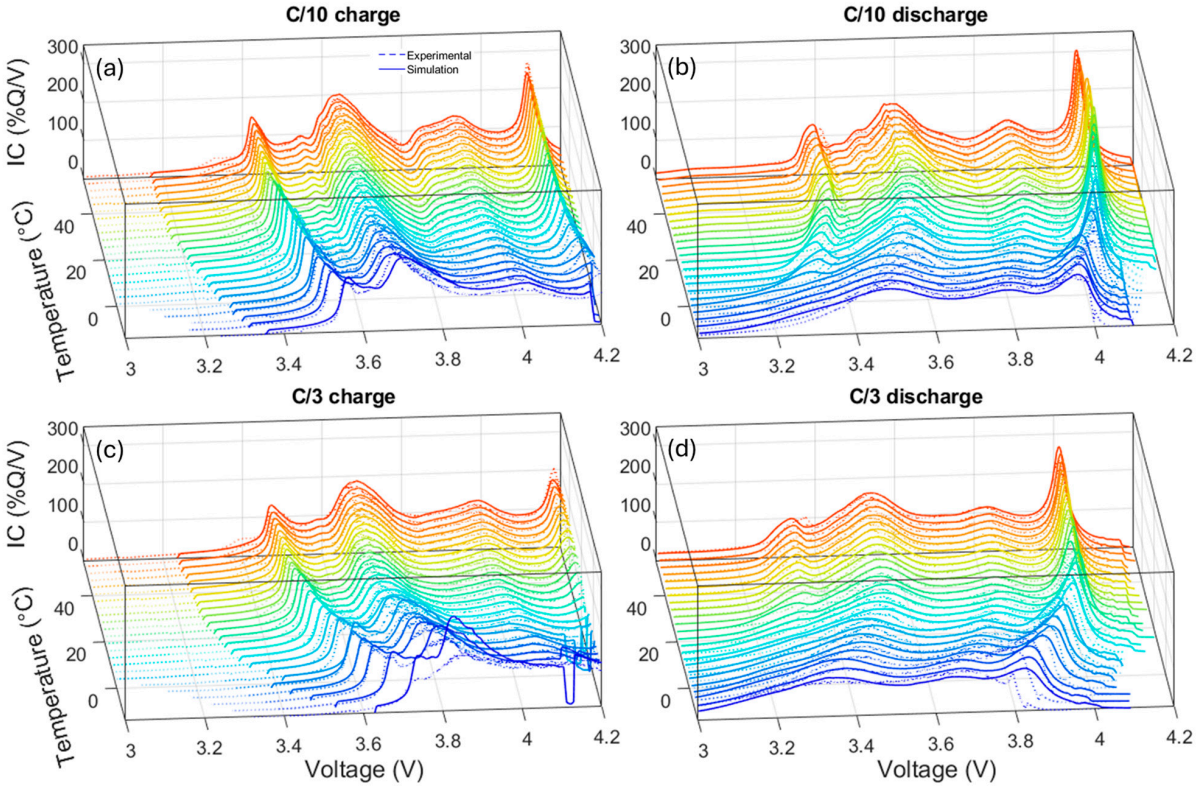


**Figure A2. NMC** cell IC signatures comparison for the experimental (dashed lines) and simulated (full lines) (**a**) C/10 charges, (**b**) C/10 discharges, (**c**) C/3 charges, and (**d**) C/3 discharges.

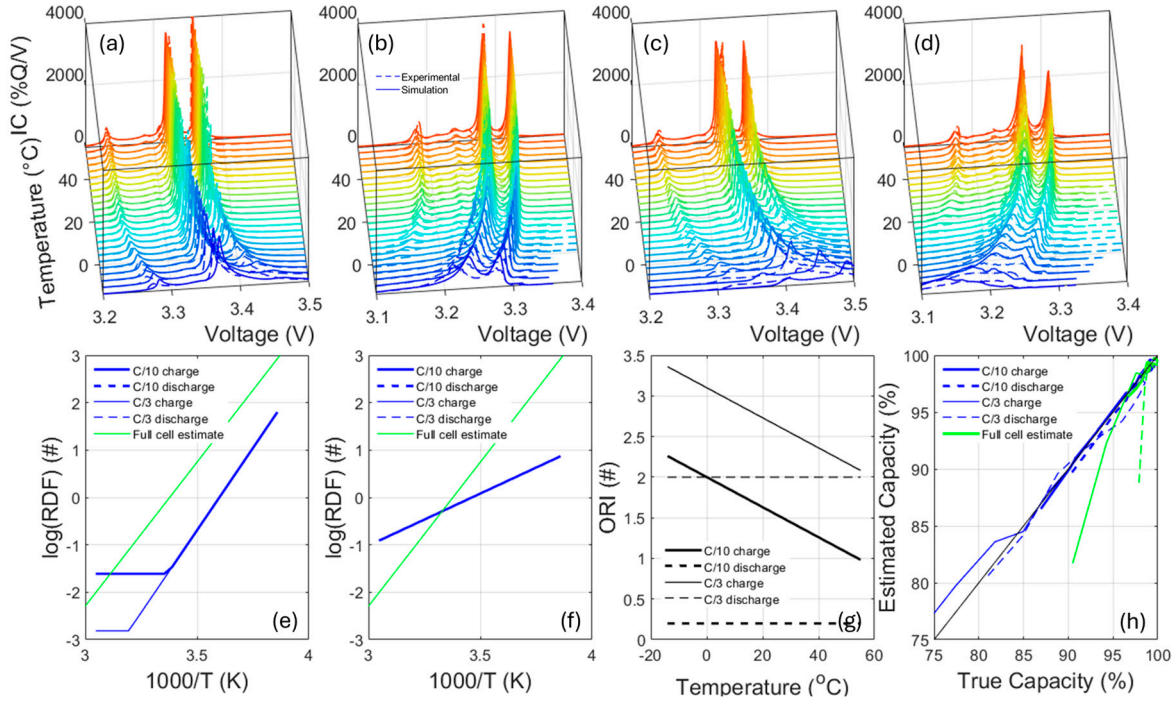


**Figure A3.** Simulated temperature emulation results from the average RDFs and varying ORIs with associated parameter variations for the LFP cell. IC signatures for the experimental (dashed lines) and simulated (full lines) (**a**) C/10 charges, (**b**) C/10 discharges, (**c**) C/3 charges, and (**d**) C/3 discharges with associated (**e**) $RDF_{PE}$, (**f**) $RDF_{NE}$, (**g**) ORI, and (**h**) capacity estimations vs. true capacity with a 1:1 line in black. Green lines correspond to the full cell-level parameters [37].

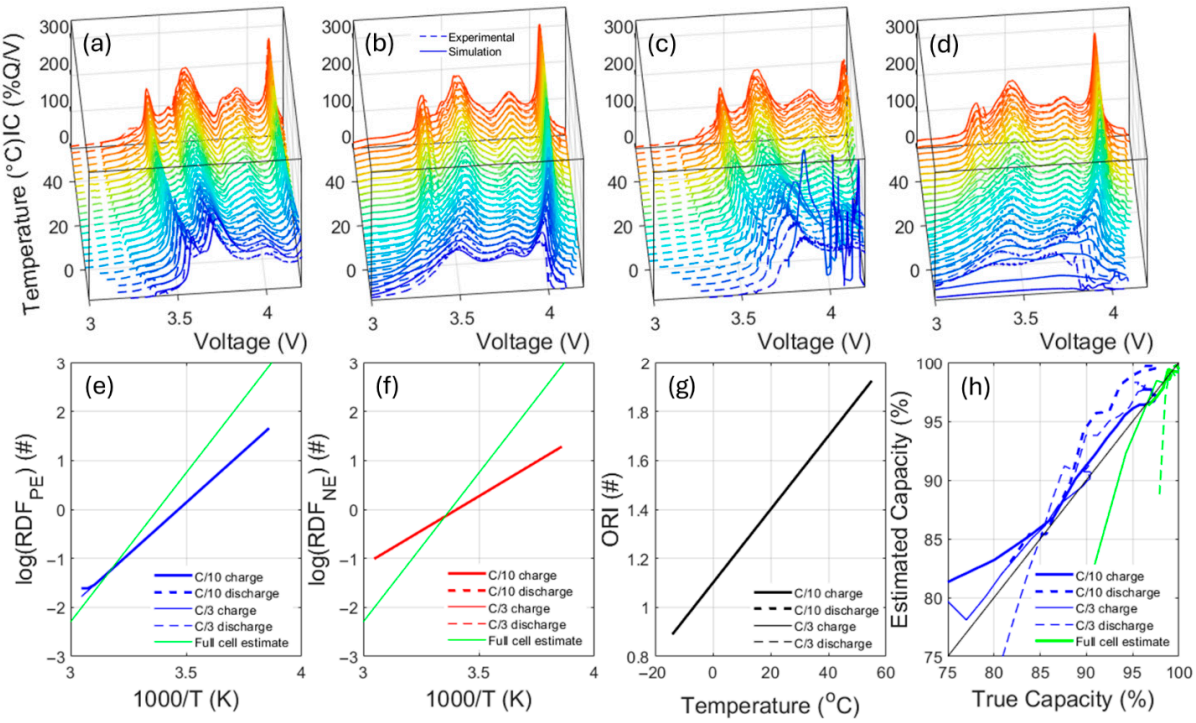


**Figure A4.** Simulated temperature emulation results from the average RDFs and ORI with associated parameter variations for the NMC cell. IC signatures for the experimental (dashed lines) and simulated (full lines) (**a**) C/10 charges, (**b**) C/10 discharges, (**c**) C/3 charges, and (**d**) C/3 discharges with associated (**e**) $RDF_{PE}$, (**f**) $RDF_{NE}$, (**g**) ORI, and (**h**) capacity estimations vs. true capacity, with a 1:1 line in black. Green lines correspond to the parameters deciphered at the full-cell level in [37].

## References

1. Hamar, J.; Sturm, J.; Jossen, A.; Erhard, S.V. Investigating the path dependent aging behavior of nickel cobalt aluminum oxide cathode batteries during high C-rate cycling conditions. *J. Electrochem. Soc.* **2024**, *171*, 020555. [CrossRef]
2. Röder, F.; Ramasubramanian, S. A Review and Perspective on Path Dependency in Batteries. *Energy Technol.* **2022**, *10*, 2200627. [CrossRef]
3. Raj, T.; Wang, A.A.; Monroe, C.W.; Howey, D.A. Investigation of Path-Dependent Degradation in Lithium-Ion Batteries. *Batter. Supercaps* **2020**, *3*, 1377–1385. [CrossRef]
4. Yang, B.; Qian, Y.; Li, Q.; Chen, Q.; Wu, J.; Luo, E.; Xie, R.; Zheng, R.; Yan, Y.; Su, S.; et al. Critical summary and perspectives on state-of-health of lithium-ion battery. *Renew. Sustain. Energy Rev.* **2024**, *190*, 114077. [CrossRef]
5. Kumar, R.; Das, K. Lithium battery prognostics and health management for electric vehicle application—A perspective review. *Sustain. Energy Technol. Assess.* **2024**, *65*, 103766. [CrossRef]
6. Demirci, O.; Taskin, S.; Schaltz, E.; Acar Demirci, B. Review of battery state estimation methods for electric vehicles-Part II: SOH estimation. *J. Energy Storage* **2024**, *96*, 112703. [CrossRef]
7. Roy, P.K.; Shahjalal, M.; Shams, T.; Fly, A.; Stoyanov, S.; Ahsan, M.; Haider, J. A Critical Review on Battery Aging and State Estimation Technologies of Lithium-Ion Batteries: Prospects and Issues. *Electronics* **2023**, *12*, 4105. [CrossRef]
8. Pratap Singh, S.; Prakash Singh, P.; Niwas Singh, S.; Tiwari, P. State of charge and health estimation of batteries for electric vehicles applications: Key issues and challenges. *Glob. Energy Interconnect.* **2021**, *4*, 145–157. [CrossRef]
9. Gismero, A.; Dubarry, M.; Guo, J.; Stroe, D.-I.; Schaltz, E. The Influence of Testing Conditions on State of Health Estimations of Electric Vehicle Lithium-Ion Batteries Using an Incremental Capacity Analysis. *Batteries* **2023**, *9*, 568. [CrossRef]
10. Zhou, H.; Fear, C.; Carter, R.E.; Love, C.T.; Mukherjee, P.P. Correlating lithium plating quantification with thermal safety characteristics of lithium-ion batteries. *Energy Storage Mater.* **2024**, *66*, 103214. [CrossRef]
11. Naylor Marlow, M.; Chen, J.; Wu, B. Degradation in parallel-connected lithium-ion battery packs under thermal gradients. *Commun. Eng.* **2024**, *3*, 1. [CrossRef]
12. Li, S.; Zhang, C.; Zhao, Y.; Offer, G.J.; Marinescu, M. Effect of thermal gradients on inhomogeneous degradation in lithium-ion batteries. *Commun. Eng.* **2023**, *2*, 74. [CrossRef]

13. Du, X.; Hu, Y.; Song, M.; Choi, C.; Choe, S.-Y.; Labaza, C.; Gao, J.; Koch, B.J.; Garrick, T.R. Experimental studies of effects of temperature gradients on performance of pouch type large format NMC/C lithium-ion battery. *J. Power Sources* **2023**, *587*, 233688. [CrossRef]
14. Fear, C.; Parmananda, M.; Kabra, V.; Carter, R.; Love, C.T.; Mukherjee, P.P. Mechanistic underpinnings of thermal gradient induced inhomogeneity in lithium plating. *Energy Storage Mater.* **2021**, *35*, 500–511. [CrossRef]
15. Carter, R.; Kingston, T.A.; Atkinson, R.W.; Parmananda, M.; Dubarry, M.; Fear, C.; Mukherjee, P.P.; Love, C.T. Directionality of thermal gradients in lithium-ion batteries dictates diverging degradation modes. *Cell Rep. Phys. Sci.* **2021**, *2*, 100351. [CrossRef]
16. Dubarry, M.; Tun, M.; Baure, G.; Matsuura, M.; Rocheleau, R.E. Battery Durability and Reliability under Electric Utility Grid Operations: Analysis of On-Site Reference Tests. *Electronics* **2021**, *10*, 1593. [CrossRef]
17. Mussa, A.S.; Smith, A.J.; Trippetta, G.M.; Lindbergh, G.; Klett, M.; Lindström, R.W. Performance and aging of a lithium-ion battery in a non-uniform temperature distribution condition. *J. Energy Storage* **2025**, *114*, 115869. [CrossRef]
18. Yu, C.; Zhu, J.; Wei, X.; Dai, H. Research on Temperature Inconsistency of Large-Format Lithium-Ion Batteries Based on the Electrothermal Model. *World Electr. Veh. J.* **2023**, *14*, 271. [CrossRef]
19. Nikolov, N.I.; Chahbaz, A.; Hildenbrand, F.; Kateri, M.; Sauer, D.U. Statistical investigation of temperature-dependent cycle lifetime and cell-to-cell variance in lithium-ion batteries: A model-based approach. *J. Power Sources* **2024**, *623*, 235334. [CrossRef]
20. Wu, B.; Yufit, V.; Marinescu, M.; Offer, G.J.; Martinez-Botas, R.F.; Brandon, N.P. Coupled thermal–electrochemical modelling of uneven heat generation in lithium-ion battery packs. *J. Power Sources* **2013**, *243*, 544–554. [CrossRef]
21. Choi, M.; Du, X.; Choe, S.-Y.; Garrick, T.R. Effect of temperature gradients in large-format pouch-type NMC/graphite lithium-ion battery on degradation. *J. Power Sources* **2026**, *677*, 240007. [CrossRef]
22. Li, Y.; Li, K.; Shen, W.; Huang, J.; Qu, X.; Zhang, Y.; Lin, Y. Stress-dependent capacity fade behavior and mechanism of lithium-ion batteries. *J. Energy Storage* **2024**, *86*, 111165. [CrossRef]
23. Luo, P.; Li, P.; Ma, D.; Wang, K.; Zhang, H. A Novel Capacity Fade Model of Lithium-Ion Cells Considering the Influence of Stress. *J. Electrochem. Soc.* **2021**, *168*, 090537. [CrossRef]
24. Xu, J.; Liu, B.; Wang, X.; Hu, D. Computational model of 18650 lithium-ion battery with coupled strain rate and SOC dependencies. *Appl. Energy* **2016**, *172*, 180–189. [CrossRef]
25. Wang, J.; Du, J.; Tan, B.; Cao, X.; Qu, C.; Ou, Y.; He, X.; Xiong, L.; Tu, R. Establishment of a Lithium-Ion Battery Model Considering Environmental Temperature for Battery State of Charge Estimation. *J. Electrochem. Soc.* **2023**, *170*, 120507. [CrossRef]
26. Tomaszewska, A.; Parkes, M.; Doel, R.; Offer, G.; Wu, B. The Effects of Temperature and Cell Parameters on Lithium-Ion Battery Fast Charging Protocols: A Model-Driven Investigation. *J. Electrochem. Soc.* **2022**, *169*, 060542. [CrossRef]
27. Mohtat, P.; Lee, S.; Sulzer, V.; Siegel, J.B.; Stefanopoulou, A.G. Differential Expansion and Voltage Model for Li-ion Batteries at Practical Charging Rates. *J. Electrochem. Soc.* **2020**, *167*, 110561. [CrossRef]
28. Jung, S.; Kang, D. Multi-dimensional modeling of large-scale lithium-ion batteries. *J. Power Sources* **2014**, *248*, 498–509. [CrossRef]
29. Waldmann, T.; Gorse, S.; Samtleben, T.; Schneider, G.; Knoblauch, V.; Wohlfahrt-Mehrens, M. A Mechanical Aging Mechanism in Lithium-Ion Batteries. *J. Electrochem. Soc.* **2014**, *161*, A1742–A1747. [CrossRef]
30. Madani, S.S.; Ziebert, C.; Marzband, M. Thermal Behavior Modeling of Lithium-Ion Batteries: A Comprehensive Review. *Symmetry* **2023**, *15*, 1597. [CrossRef]
31. Dubarry, M.; Truchot, C.; Liaw, B.Y. Synthesize battery degradation modes via a diagnostic and prognostic model. *J. Power Sources* **2012**, *219*, 204–216. [CrossRef]
32. Honkura, K.; Honbo, H.; Koishikawa, Y.; Horiba, T. State Analysis of Lithium-Ion Batteries Using Discharge Curves. *ECS Trans.* **2008**, *13*, 61–73. [CrossRef]
33. Dahn, H.M.; Smith, A.J.; Burns, J.C.; Stevens, D.A.; Dahn, J.R. User-Friendly Differential Voltage Analysis Freeware for the Analysis of Degradation Mechanisms in Li-Ion Batteries. *J. Electrochem. Soc.* **2012**, *159*, A1405–A1409. [CrossRef]
34. Bloom, I.; Jansen, A.N.; Abraham, D.P.; Knuth, J.; Jones, S.A.; Battaglia, V.S.; Henriksen, G.L. Differential voltage analyses of high-power, lithium-ion cells. 1. Technique and Applications. *J. Power Sources* **2005**, *139*, 295–303. [CrossRef]
35. Schindler, S.; Baure, G.; Danzer, M.A.; Dubarry, M. Kinetics accommodation in Li-ion mechanistic modeling. *J. Power Sources* **2019**, *440*, 227117. [CrossRef]
36. Dubarry, M.; Beck, D. Perspective on Mechanistic Modeling of Li-Ion Batteries. *Acc. Mater. Res.* **2022**, *3*, 843–853. [CrossRef]
37. Fernando, A.; Dubarry, M. Model-free emulation of the impact of kinetics and temperature on commercial Li-ion batteries. *J. Power Sources* **2025**, *654*, 237796. [CrossRef]
38. Iaboni, D.S.M.; Obrovac, M.N. Li15Si4Formation in Silicon Thin Film Negative Electrodes. *J. Electrochem. Soc.* **2015**, *163*, A255–A261. [CrossRef]
39. Dubarry, M.; Anseán, D. Best practices for incremental capacity analysis. *Front. Energy Res.* **2022**, *10*, 1023555. [CrossRef]
40. McBrayer, J.D.; Harrison, K.L.; Allcorn, E.; Minteer, S.D. Chemical contributions to silicon anode calendar aging are dominant over mechanical contributions. *Front. Batter. Electrochem.* **2023**, *2*, 1308127. [CrossRef]

41. McBrayer, J.D.; Rodrigues, M.-T.F.; Schulze, M.C.; Abraham, D.P.; Apblett, C.A.; Bloom, I.; Carroll, G.M.; Colclasure, A.M.; Fang, C.; Harrison, K.L.; et al. Calendar aging of silicon-containing batteries. *Nat. Energy* **2021**, *6*, 866–872. [CrossRef]
42. Waldmann, T.; Innocenti, A.; Scheck, V.; Bischof, K.; Feser, R.V.; Moosmann, P.; Kasper, M.; Marinaro, M.; Hoffmann, A.; Wohlfahrt-Mehrens, M.; et al. From Laboratory to Application—Differences between Small and Large Battery Cells. *J. Electrochem. Soc.* **2026**, *173*, 050501. [CrossRef]
43. Wu, L.; Liu, K.; Liu, J.; Pang, H. Evaluating the heat generation characteristics of cylindrical lithium-ion battery considering the discharge rates and N/P ratio. *J. Energy Storage* **2023**, *64*, 107182. [CrossRef]
44. Liu, J.; Chavan, S.; Kim, S.-C. Investigation of the Electrochemical and Thermal Characteristics of NCM811-21700 Cylindrical Lithium-Ion Battery: A Numerical Study and Model Validation. *Energies* **2023**, *16*, 6407. [CrossRef]
45. HNEI. Alawa Central. Available online: https://www.hnei.hawaii.edu/alawa (accessed on 1 May 2026).

**Disclaimer/Publisher's Note:** The statements, opinions and data contained in all publications are solely those of the individual author(s) and contributor(s) and not of MDPI and/or the editor(s). MDPI and/or the editor(s) disclaim responsibility for any injury to people or property resulting from any ideas, methods, instructions or products referred to in the content.